

# Fracture phenomenology of a sintered silicon nitride containing oxide additives

R. K. GOVILA

*Materials Engineering Department, Scientific Research Laboratory, Ford Motor Company, PO Box 2053, Dearborn, Michigan 48121, USA*

Crack propagation mechanisms in a sintered silicon nitride containing various oxide additives (ceria, magnesia, zirconia and strontium oxide) were studied as a function of initial flaw size, temperature, applied stress and time. Surface cracks of controlled size were introduced using the microhardness indentation-induced-flaw technique. At 20° C, the fracture stress was found to depend on initial crack size according to the Griffith relationship and extrapolation of the data indicated that processing flaws of 20 to 35  $\mu\text{m}$  were strength-controlling. The flexural strength was found to be independent of temperature from 20 to 800° C and the mode of crack propagation was primarily transgranular. At temperatures above 800° C the flexural strength decreased significantly, due to viscous flow of the glassy phase present in the material and resulting in sub-critical crack growth (SCG). The mode of crack propagation during SCG was essentially intergranular. Flexural stress-rupture evaluation in the temperature range 800 to 1000° C has identified the stress levels for time-dependent and time-independent failures.

## 1. Introduction

Silicon nitride containing various oxide additives such as yttria, ceria, magnesia, zirconia and alumina consolidated in hot-pressed and sintered form is currently being evaluated for use in structural components at high temperatures ( $\geq 1000^\circ\text{C}$ ) for gas turbines, and low temperatures ( $\leq 1000^\circ\text{C}$ ) for diesel engines, because of its high strength and good thermal shock resistance. A need exists for a ceramic material which can combine strength with a near-net-shape fabrication process. The hot-pressed material is limited in commercial use to simple shapes like solid circular discs and rectangular or triangular pieces like cutting-tool inserts. Structural engine components like turbine rotors and stators cannot be fabricated to net shape by hot-pressing methods, and machining from hot-pressed billets is too expensive and time-consuming. In contrast, sintered material offers an advantage over the hot-pressed material since many structural components can be fabricated using commercial injection-moulding or slip-casting techniques. Under suitable conditions (time, temperature, pressure and environment), engine parts can be sintered to full density provided allowance is made for sintering shrinkages. Like many other ceramics, sintered silicon nitride is generally regarded as a brittle material with little tolerance, from a structural viewpoint, to incipient flaws (primarily porosity) which are present due to processing and fabrication.

The objective of the present work was to determine quantitatively and qualitatively the susceptibility of a commercially available sintered silicon nitride (NGK-SN73) material containing several oxide additives (ceria, magnesia, zirconia and strontium oxide) to

brittle (catastrophic) fracture and time-dependent failure from inherent processing flaws, and to evaluate the crack propagation mechanisms operative over a temperature range of practical use (800 to 1200° C). In this paper, we report the results of a series of simple mechanical tests performed on as-machined and precracked flexural specimens to measure the bend strength of sintered silicon nitride (NGK-SN73) as a function of flaw size, temperature, applied stress and time. Estimates of the size of strength-controlling flaws in the as-processed and machined material, and the fracture energy,  $\gamma$ , for brittle failure, have been determined. In addition, long-term reliability and durability were characterized using flexural stress rupture testing in the temperature range 800 to 1000° C. Fractography is used as the principal interpretive agent for the presence of sub-critical crack growth (SCG) and in revealing the mechanistic aspects of crack propagation.

## 2. Material and experimental techniques

### 2.1. Material

The material used in this study was sintered silicon nitride commercially known as SN-73 (NGK Insulators Ltd, Nagoya, Japan) obtained in the form of a cylinder (length = 138 mm, inside and outside diameters 80 and 100 mm, respectively). The sintered silicon nitride contained various oxide additives ( $\text{CeO}_2$ ,  $\text{MgO}$ ,  $\text{ZrO}_2$  and  $\text{SrO}$ ) as sintering aids, and had a density of  $3.26\text{ g cm}^{-3}$ . The typical chemical composition as provided by the manufacturer is given in Table I.

The test component (cylinder) was isostatically pressed and contained an organic binder. The burn-

TABLE I Chemical composition of sintered silicon nitride (NGK-SN73)

	Ceria	MgO	ZrO <sub>2</sub>	SrO	Silicon nitride
Parts by weight	5	4	3	1	100

out of the component was carried out at 150 to 225°C in a nitrogen gas environment and finally pressureless sintered at 1700°C. Complete processing details are given elsewhere [1]. X-ray diffraction of the as-machined bulk sample revealed primarily  $\beta$ -Si<sub>3</sub>N<sub>4</sub> and traces of glass.

## 2.2. Specimen preparation and testing (fast fracture and stress rupture)

Flexural test specimens (approximately 32 mm long  $\times$  6 mm wide  $\times$  3 mm thick) were machined from the cylinder (test component) wall. All faces were ground lengthwise using 320 grit diamond wheels; the edges were chamfered (lengthwise) to prevent notch effects. Complete details of flexural strength evaluation (in a fast fracture mode) at room temperature and above (800 to 1200°C), flexural stress rupture testing at elevated temperatures (800 to 1000°C) in an air environment, self-aligning ceramic test fixture and test-span dimensions have been reported previously [2, 3].

## 2.3. Indentation-induced-flaw technique

Test specimens used in this technique were identical to those used for flexural strength evaluation except that

these were precracked using the Vickers diamond pyramid and Knoop microhardness indenters (Wilson Instrument Division, ACCO, Bridgeport, Connecticut) and tested in a similar fashion to the previous specimens. Indenting the sintered silicon nitride with a Vickers and Knoop indenter resulted in the introduction of surface cracks, the geometry and size (depth of crack) of which were controlled by the choice of indenter load and microstructure of the sintered material. It should be pointed out that even though all precracked specimens tested at 20°C failed at the precrack site, the crack fronts on the fracture surfaces were not clearly visible and crack depths could not be measured accurately. For various indentation loads used, the corresponding surface crack lengths as seen optically were measured. Assuming the crack fronts to be semi-circular, the crack depths were estimated. A schematic representation of crack geometry in a test specimen and details of the indentation-induced-flaw (IIF) technique have been reviewed earlier [3-7]. All precracking was done at room temperature on as-machined surfaces of flexural test specimen.

## 3. Results and discussion

### 3.1. Fracture energy and flaw-size estimate

A series of specimens was prepared and precracked with microhardness indentation loads ranging from 1000 to 4000 g. The variation of fracture stress with crack depth (actually the inverse square root of crack depth) for precracked specimens tested at 20°C is shown in Fig. 1. Although there is considerable scatter in the data (see Table II), a reasonably good linear relation is evident which correlates with the Griffith [8]

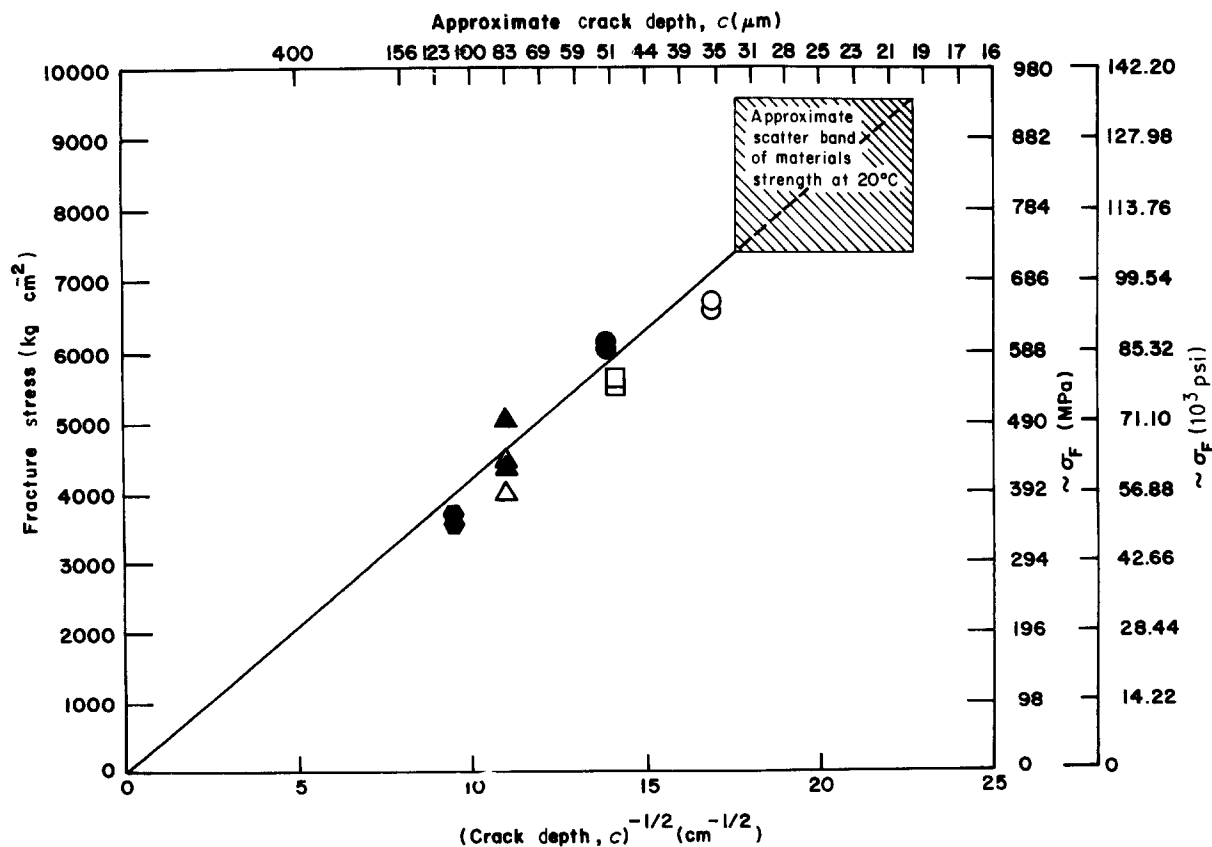


TABLE II Flexural strength results for precracked sintered silicon nitride (NGK-SN73)

Indentation load (g)	Test temperature (°C)	Approximate crack depth (μm)	Fracture stress (MPa)	Remarks
<i>Vickers indenter</i>				
1000	20	35	661	Failed at the precrack site.
1000	20	35	648	Failed at the precrack site.
2000	20	50	553	Failed at the precrack site.
2000	20	50	544	Failed at the precrack site.
4000	20	80	393	Failed at the precrack site.
4000	20	80	439	Failed at the precrack site.
4000	20	80	439	Failed at the precrack site.
4000	1000	80	413	Failed at the precrack site.
4000	1200	80	331	Did not fail at the precrack site and showed SCG from corner.
<i>Knoop indenter</i>				
1000	20	52	604	Failed at the precrack site.
1000	20	52	593	Failed at the precrack site.
2000	20	80	494	Failed at the precrack site.
2000	20	80	426	Failed at the precrack site.
4000	20	112	351	Failed at the precrack site.
4000	20	112	364	Failed at the precrack site.
1000	1200	52	323	Did not fail at the precrack site and showed SCG region.
2000	1200	80	323	Did not fail at the precrack site and showed SCG from corner.
4000	1200	100	336	Failed at the precrack site and showed extensive SCG (Fig. 7).

criterion for brittle fracture:

$$\sigma_F \approx Y[E\gamma/c]^{1/2} \quad (1)$$

where  $\sigma_F$  is the fracture stress required to propagate a pre-existing crack of known dimensions,  $Y$  is a constant relating primarily to crack geometry and specimen dimensions,  $E$  is Young's modulus,  $c$  is the initial crack depth at which fracture initiated, and  $\gamma$  is the fracture energy. For approximately semicircular cracks (as shown later) and for simplicity,  $Y$  is taken as unity. For a value of  $E = 234$  GPa [9] at 20°C, and the slope of the curve shown in Fig. 1, the computed value of fracture energy,  $\gamma$ , is approximately  $73 \text{ J m}^{-2}$  ( $73\,000 \text{ erg cm}^{-2}$ ) at 20°C. It is imperative to note, however, that the above can be taken rigorously only as a demonstration of principle. The presence of residual stresses (tensile at the crack front) at microhardness indentation sites has been suggested by several investigators as discussed elsewhere [3–7]. It is important to realize that the presence of such stresses could significantly influence the absolute magnitude of the experimentally determined fracture energy.

From a practical point of view, perhaps the most useful application of the data shown in Fig. 1 is as a means of estimating the flaw size in “as-machined” sintered silicon nitride. Extrapolation of the data in Fig. 1 to the fracture stress of uncracked (as-machined) test samples (shown as the approximate scatter band of materials strength) indicates that flaws of the order of 20 to 35 μm are present in the as-processed sintered silicon nitride. This theoretical prediction about the flaw size was in fact confirmed in several test specimens where failure origins and randomly occur-

ring flaws in the material were close to the predicted size, as shown in Figs 2 and 3.

### 3.2. Flexural strength and its variation with temperature

At 20°C, a total of ten specimens were tested in four-point bending in order to determine the fast fracture strength ( $\sigma_f$ ). The material showed a large scatter in  $\sigma_f$ , possibly due to large variations in processing flaw sizes.  $\sigma_f$  varied from a minimum of 729 MPa to a maximum of 933 MPa with an average strength of 790 MPa (standard deviation 91 MPa) and Weibull modulus  $m = 10.4$ . Earlier [9] strength evaluation of the same material from the manufacturer's laboratory (NGK Insulators), using a total of 50 test bars,<sup>†</sup> proved the average  $\sigma_f$  at 20°C to be 880 MPa and a Weibull modulus  $m = 14$ . A recent study from the manufacturer's laboratory by Soma *et al.* [10] on the same material (NGK-SN73) using a larger data base (200 test samples) and different specimen size<sup>†</sup> reported an average strength of 802 MPa with a Weibull modulus  $m = 19$ . The low and high values were 559 and 908 MPa, respectively. It is important to note the large variations in  $\sigma_f$  and Weibull modulus as displayed by this study and that of the NGK laboratories strongly suggest non-uniformity and inhomogeneity in composition and microstructure of the material. In addition, the low value of Weibull modulus,  $m = 10$ , obtained in this study may be a true reflection of the flaw size variation and reproducibility of the material as the test specimen were cut from an engine test component (cylinder).

Examination of the as-machined and fracture

<sup>†</sup> Test samples were 40 mm long × 4 mm wide × 3 mm thick, tested in four-point bending with an outer and inner span of 30 and 10 mm, respectively. A machine crosshead speed of  $0.5 \text{ mm min}^{-1}$  was used.

surfaces in this study revealed failure-initiating sites as surface (Fig. 2) and sub-surface porosity (Fig. 3), flaws associated with processing contaminants such as glassy material (Fig. 2) and metallic (iron) inclusions (see later). Failure-initiating porous regions varied in size, ranging from 30 to 60  $\mu\text{m}$  long and 10 to 40  $\mu\text{m}$  wide, circular, semi-circular or ellipsoidal in shape (Fig. 3b). Closer examination of the flaw site revealed that the grain morphology of  $\beta\text{-Si}_3\text{N}_4$  inside the porous region is primarily needle-shaped (acicular) (Fig. 3c), and less acicular away from it (Fig. 3d). The presence of such large porous regions suggests that full densification of the bulk material did not occur during sintering. From the fractographs, it appears that the primary mode of crack propagation during fast fracture (catastrophic failure) was primarily transgranular, and sometimes a mixed mode of fracture consisting of transgranular and intergranular crack growth. In spite of large variations in strength, it appears that sintered silicon nitride containing several oxide additives can be fabricated to yield high strength (790 MPa) at 20°C, and the strength can be significantly improved by optimizing the sintering conditions and minimizing the presence of metallic inclusions.

Flexural strength was also evaluated at higher temperatures (800 to 1200°C) and the variation in

strength as a function of temperature is shown in Fig. 4. Five specimens were tested at 800°C and each failed above 800 MPa, showing a small increase in  $\sigma_f$  relative to room-temperature strength. This small increase in  $\sigma_f$  at 800°C is believed to be due to early softening of the glassy phase present in the material, thereby blunting the randomly distributed flaws. The presence of glass was clearly visible in tests made at 1000 to 1200°C, thus confirming the above hypothesis. In short,  $\sigma_f$  can be considered independent of temperature up to about 800°C (Fig. 4). The constancy of  $\sigma_f$  in this temperature range implies that a single fracture mechanism predominates, and that insignificant plastic deformation (viscous flow due to glass formation) accompanied the fracture process.

A small decrease in  $\sigma_f$  was noted at 900°C relative to room-temperature strength. A typical fracture surface showing failure occurring at a metallic inclusion (iron particles) is shown in Fig. 5. Even though fracture surfaces did not show the presence of the glassy phase or the occurrence of SCG possibly due to fast fracture testing, it is believed that the decreased strength at 900°C was due to limited creep deformation causing large voids or cavity formation surrounding the flaw site.

A sudden and sharp drop in  $\sigma_f$  was noticed in tests made at 1000°C and above,  $\sigma_f$  decreased to almost one-half the room temperature strength (Fig. 4). A typical fracture surface for a specimen tested in a fast fracture mode at 1000°C is shown in Fig. 6. The semicircular region ACB, whose boundary has been identified by the arrows in Fig. 6a, appears to be the slow crack growth region. Closer examination inside the SCG region revealed the shape and morphology of the failure-initiating flaw EDF (Figs 6b and c), as a long (30 to 40  $\mu\text{m}$ ) and narrow (10 to 15  $\mu\text{m}$  wide) porous region. The presence of gas bubbles (air or nitrogen) trapped in the viscous flow of the glassy phase present in the material was visible (indicated by

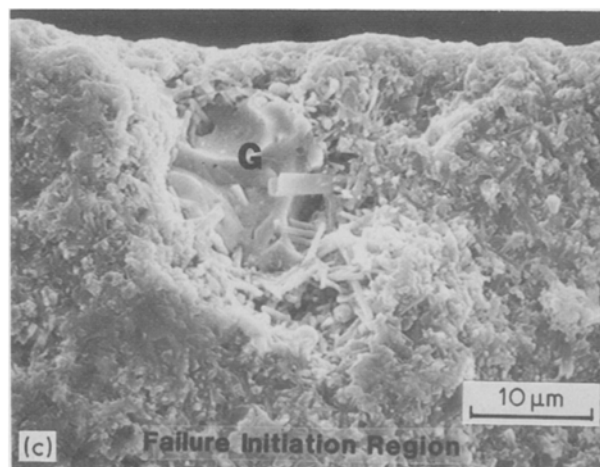
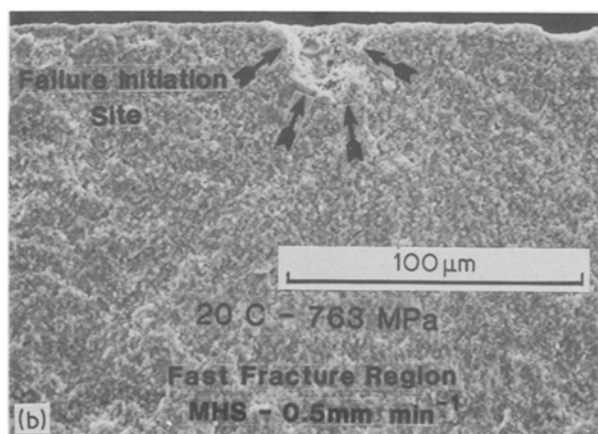


Figure 2 SEM micrographs of sintered silicon nitride (NGK-SN73). (a) Randomly distributed porosity ranging in size from 1 to 10  $\mu\text{m}$  seen in as-machined surface at 20°C. Often these pores (or flaws) are interlinked and thus result in a longer effective surface flaw. Arrows indicate the direction of machining; (b, c) Surface-associated failure (40 to 45  $\mu\text{m}$  wide and 25 to 30  $\mu\text{m}$  deep). "G" indicates the presence of glassy-phase material.

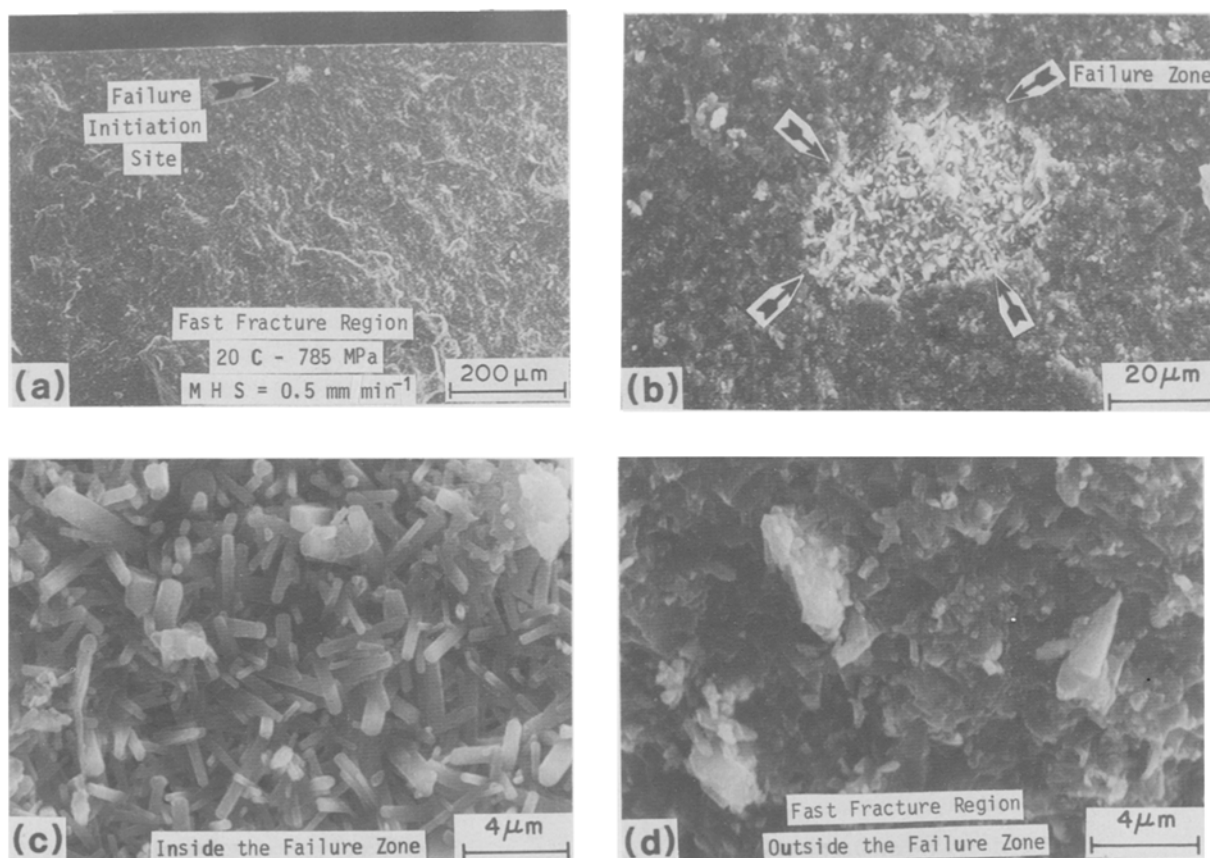


Figure 3 (a–d) SEM fractographs showing failure occurring at a sub-surface porous region (ellipsoidal in shape with major and minor axis approximately 50 and 30  $\mu\text{m}$  long, respectively). MHS refers to machine head speed.

small arrows in Fig. 6b). Microstructure inside the flaw (Fig. 6c) was similar to that observed at 20°C, (Fig. 3c). The test specimen showed minor discoloration at 1000°C. Similar behaviour but an increased viscous flow of the glassy phase and oxidation were observed at 1200°C (Fig. 7). The fracture surface showed a large, localized SCG region as the failure zone. The SCG region ACB (Fig. 7a) is distinct in its appearance, being characterized by a rough surface.

The mode of fracture during SCG is primarily intergranular as discussed later for the stress rupture tests. Up to 1100°C, the load–deflection or load–time curves showed linear elastic behaviour and at 1200°C significant deviation from the elastic line was observed, indicative of creep deformation. Detailed strength characterization of this material has been recently reported elsewhere [11].

As mentioned earlier, fracture surfaces for precracked

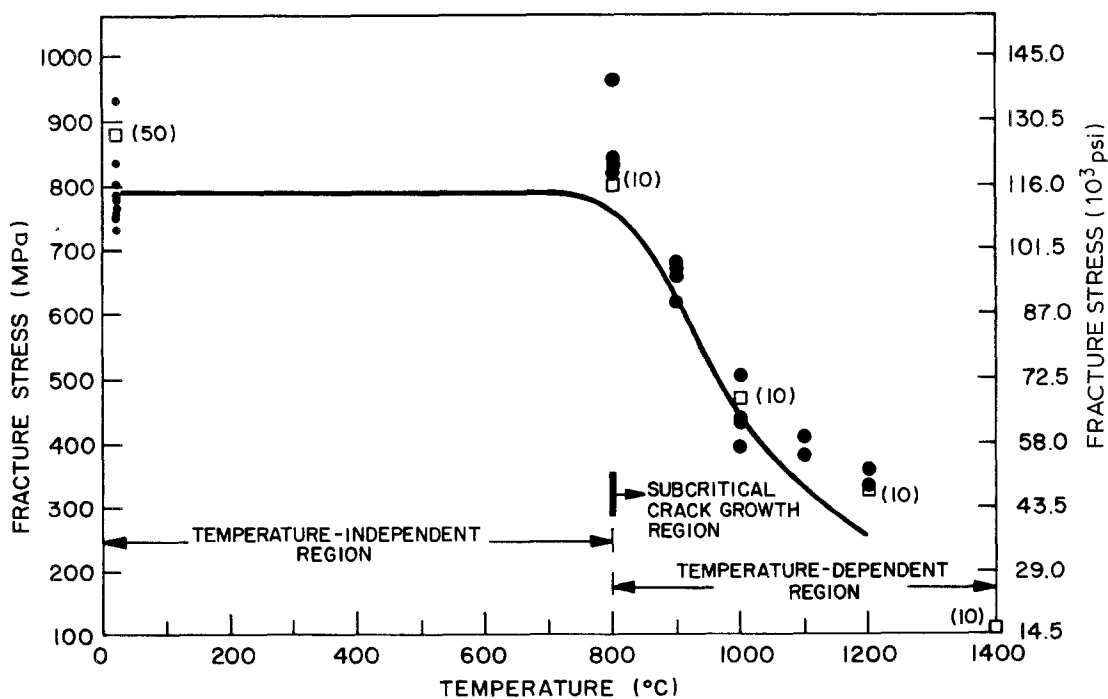


Figure 4 (●) Flexural strength (four-point bending) variation as a function of temperature; (□) manufacturer's data.

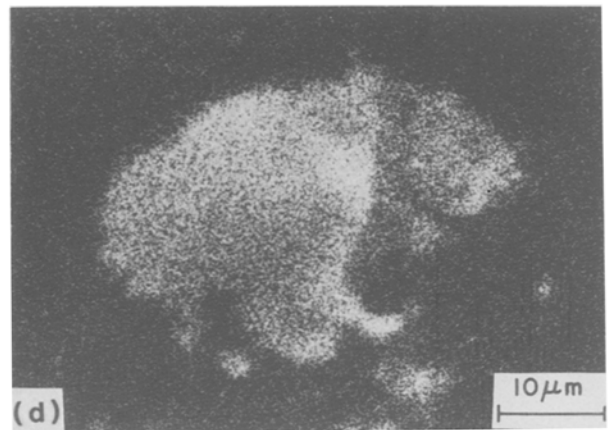
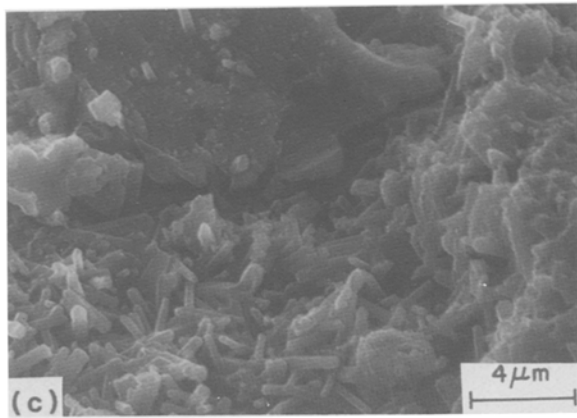
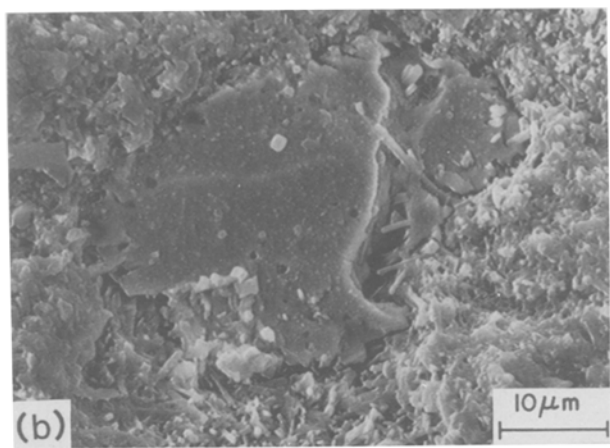
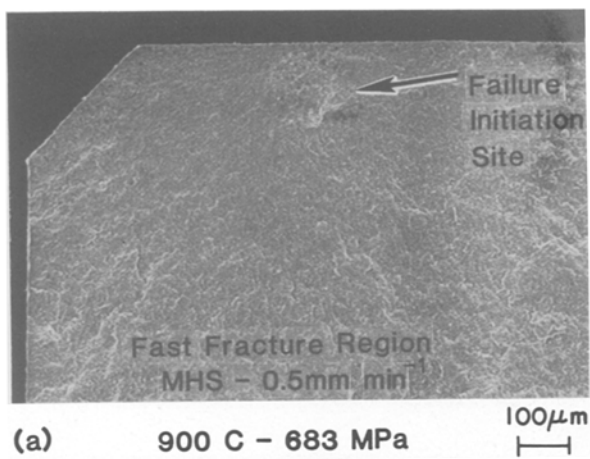
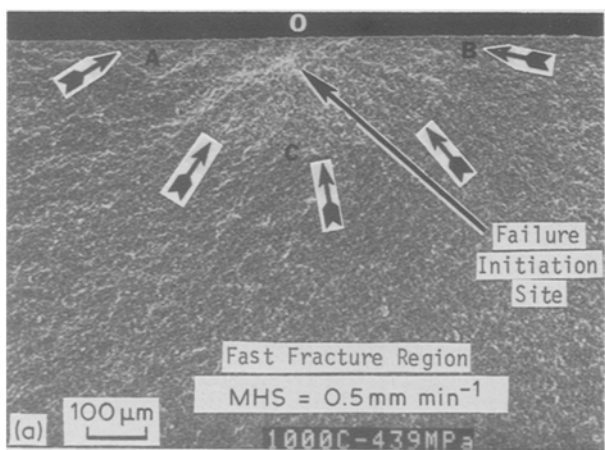


Figure 5 (a–c) SEM fractographs showing failure occurring at a metallic inclusion (iron particle,  $\sim 25 \mu\text{m}$  in width) at  $900^\circ\text{C}$ . Note cracking surrounding the inclusion. (d) X-ray map for iron using an energy-dispersive spectrometer, illustrating the concentration of iron at the inclusion site seen in (b).



specimens tested at  $20^\circ\text{C}$  did not reveal the shape and depth of the initial crack. Therefore, a few pre-cracked specimens were tested at  $1200^\circ\text{C}$  in order to reveal the crack-front geometry and depth. The results are summarized in Table II. Specimens containing cracks ranging in size from  $50$  to  $80 \mu\text{m}$  (pre-cracked with  $1000$  and  $2000 \text{ g}$  Knoop indenter) did not fail at the precrack site, possibly due to “crack blunting”. The “crack blunting” is believed to be due to viscous flow of the glassy phase present in the material

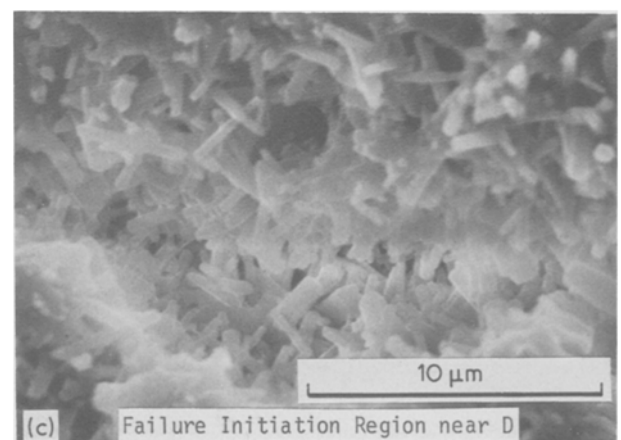
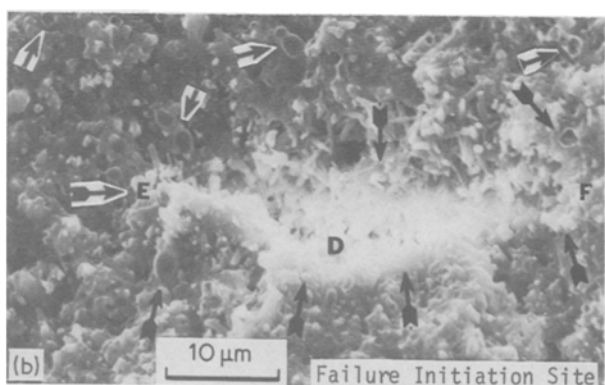


Figure 6 (a–c) SEM fractographs showing failure initiation at  $1000^\circ\text{C}$ . ACB appears to be the slow crack growth region. EDF are failure initiation sites.

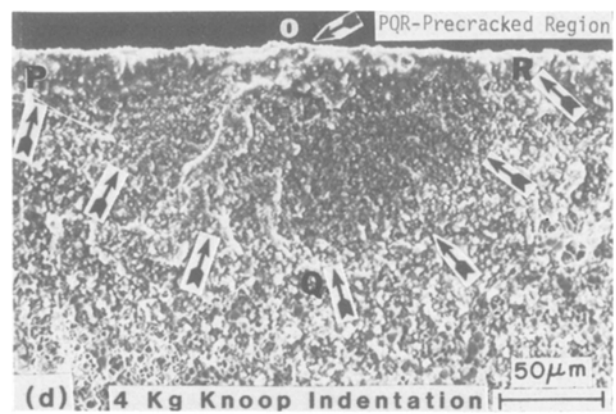
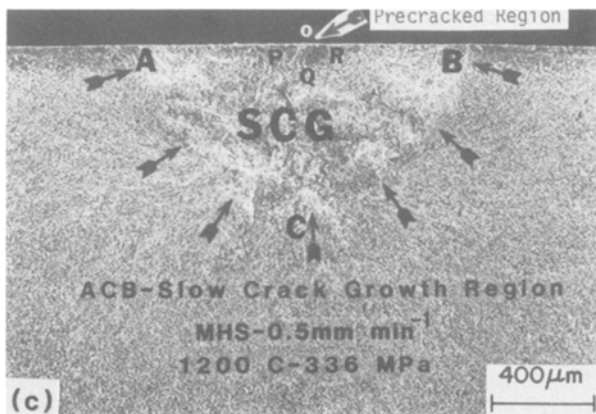
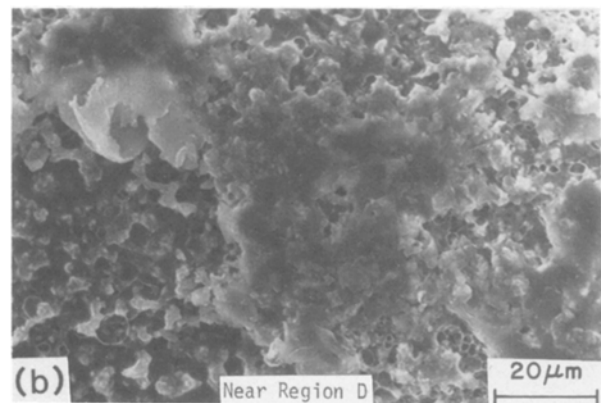
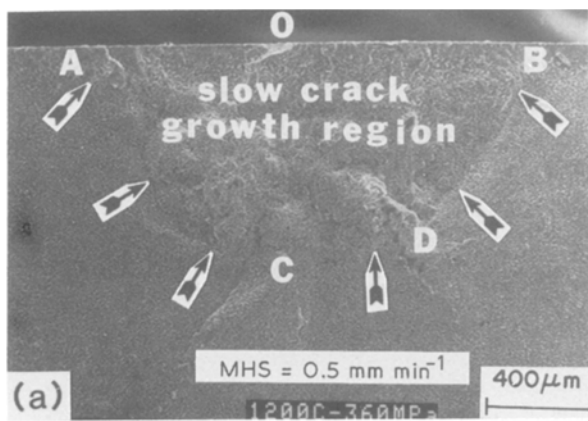


Figure 7 (a–d) SEM fractographs showing failure initiation and propagation in as-machined (a, b) and precracked (c, d) specimens tested in fast fracture mode at 1200°C. Note the development of a large SCG region [ABC] in both specimens. (PQR) precracked region.

as seen before (Figs 7a and b). It is important to note that in spite of the fact that these specimens contained cracks of significantly different size, yet the magnitude of the fracture stress (323 to 331 MPa) was essentially constant. However, when a specimen containing a slightly larger crack, say 100 to 112  $\mu\text{m}$  (precracked with 4000 g Knoop indenter), was tested at 1200°C, it failed at a stress of 336 MPa at the precrack site and showed a large region of SCG surrounding the initial crack (Figs 7c and d). Several aspects of the fracture at 1200°C in as-machined and precracked specimens merit further discussion. As-machined and precracked specimens when tested at 1200°C failed essentially at a constant stress level of about 330 MPa (see Fig. 4 and Table II), and all showed large regions of SCG of comparable size (Fig. 7). This points out the importance of the temperature in identifying that the failure at 1200°C is governed by the viscous flow of the glassy phase present in the material and is independent of the inherent flaw size.

### 3.3. Flexural stress rupture

It should be pointed out that some yttria-doped silicon nitrides consolidated in a hot-pressed or sintered condition show severe degradation of strength at intermediate temperatures (600 to 1000°C) due to both static oxidation and stress-enhanced oxidation [12–20]. The material investigated here did not contain yttria but contained another rare-earth oxide, ceria, and other oxide additives like MgO, ZrO<sub>2</sub> and SrO, and may show oxidation instability similar to that seen in yttria-doped silicon nitrides. The oxidation

kinetics and phase relations for ceria-doped silicon nitride in the hot-pressed and sintered conditions have been discussed in detail by several investigators [16, 17, 21–23]. Therefore, flexural stress rupture tests were carried out as a function of temperature (600 to 1000°C) and applied stress in order to determine (a) the material's susceptibility to low-temperature instability, (b) the presence of SCG at 800 to 1000°C, and (c) to identify allowable stress levels for a limited time ( $\leq 100$  h). A total of 30 specimens were tested in the stress rupture mode and the results are summarized in Table III.

At 600°C, two specimens were tested at applied stress levels of 413 and 482 MPa, and both sustained the stress for over 400 h without showing any signs of bending and failure. In addition, these specimens did not show any significant weight gain, suggesting the absence of static oxidation at this temperature.

At 800°C, two specimens sustained the applied stress of 344 MPa for 528 and 310 h, respectively, without showing failure and bending. As the applied stress was increased to 413 MPa, three specimens out of four failed in 175, 162 and 410 h and one sustained the stress for 235 h without failure but displayed extremely fine bending [11]. Examination of the fracture surfaces revealed the presence of SCG. A typical fracture surface for the specimen failing in 410 h is shown in Fig. 8. The SCG region is distinctly different from the remainder of the fracture surface and its boundary is marked by the arrows in Fig. 8a. SEM examination of the SCG region clearly revealed the randomly distributed failure-initiating flaws (Fig. 8b). These "flaws"

TABLE III Flexural stress rupture results for sintered silicon nitride containing various oxide additives (NGK-SN73)

Test temperature (°C)	Applied stress (MPa)	Failure time (h)	Sustained time without failure (h)	Fracture origin, discoloration*, local oxidation region (LOR), spot formation, slow crack growth (SCG), specimen bending	
600	413	—	450	No discoloration, no spot formation, no bending.	
	482	—	400	No discoloration, no spot formation, no bending.	
800	344	—	528	Minor discoloration, no spot formation, no bending.	
	344	—	310	Minor discoloration, no spot formation, no bending.	
	413	175	—	Localized SCG region, minor discoloration.	
	413	162	—	Oxidation and SCG region from corner.	
	413	410	—	Localized SCG region, minor discoloration (Fig. 8).	
	413	—	235	Minor discoloration, no spot formation, <i>shows fine bending</i> .	
	482	77	—	Surface associated porosity failure, minor discoloration.	
	482	—	216	Minor discoloration, no spot formation, <i>shows fine bending</i> .	
	482	—	266	Minor discoloration, no spot formation, <i>shows fine bending</i> .	
900	276	—	522	Discoloration and no bending.	
	344	0.2	—	Surface failure, porous region 15 $\mu\text{m}$ wide and 70 $\mu\text{m}$ deep or long.	
	344	3	—	Small SCG region, minor discoloration.	
	344	34	—	Oxidation and SCG region from corner, discoloration.	
	344	15	—	SCG from corner, minor discoloration.	
	344	—	212	Discoloration and <i>shows fine bending</i> .	
	344	—	642	Discoloration and <i>shows fine bending</i> .	
	413	0.2	—	Small SCG region, minor discoloration.	
	413	0.1	—	Surface-initiated porosity failure, minor discoloration.	
	413	0.4	—	Surface-initiated porosity failure, minor discoloration.	
	413	0.1	—	Surface-initiated porosity failure, minor discoloration.	
	1000	276	0.1	—	Inclusion, porosity, SCG region, discoloration.
		276	0.3	—	Porosity and large SCG region, discoloration (Fig. 9).
276		—	425	Discoloration, no spot formation, <i>shows fine bending</i> .	
317		0.017	—	Porosity and SCG region, minor discoloration.	
344		1	—	Oxidation and SCG region, discoloration.	
344		3	—	Oxidation and SCG region, discoloration.	
413		0.017	—	Inclusion, surface-initiated failure, discoloration.	
413		0.034	—	Metallic inclusion, oxidation, fine porosity, discoloration.	

\* As-processed material was medium grey.

are believed to be processing defects similar to that seen earlier in Fig. 6b. Inside the SCG region, the presence of a viscous glass phase and cavity formation can clearly be seen (Figs 8c and d). In addition, some fibrous structure is also visible (Fig. 8c). As the applied stress was increased to 482 MPa, the time-to-failure decreased (Table III). Three specimens were tested at 482 MPa; one failed after 77 h and the other two specimens sustained the stress for over 200 h but both displayed fine bending. At 800°C, it is believed that oxidation did not play a significant role in causing failures due to two reasons: (a) no significant weight gains were observed among those specimens which survived over 200 h duration (Table III), and (b) fracture surfaces did not reveal any penetration of localized or preferential oxygen diffusion areas suggesting oxide-related failures [19, 20].

At 900°C and 344 MPa, a total of six specimens were tested. One specimen failed in 0.2 h due to a large-size processing flaw [11]. Three specimens failed in relatively short duration, the time-to-failure ranging from 3 to 44 h, and displayed the presence of limited SCG. Two specimens sustained the stress for 212 and 642 h without failure but displayed fine bending. As the applied stress was increased to 413 MPa, the time-to-failure decreased significantly as displayed by four specimens failing between 0.1 to 0.4 h. All failures in these specimens originated at processing defects like porous regions and glassy material.

It should be pointed out that similar stress rupture studies [24] on the same material (NGK-SN73) at 800 and 900°C have been carried out in the manufacturer's laboratory and the results differ significantly from those reported in this study. For example, at 800°C and an applied stress of 450 MPa, three specimens were tested and sustained the stress for 730, 1000 and 1200 h without failure. At 900°C, two specimens were tested at 400 and 350 MPa and failed in 160 and 800 h, respectively. These differences can only be explained on the basis that the material evaluated by the NGK Insulators [24] is possibly different in chemical composition, phases and microstructure from the material used in making the component (cylinder) supplied to us. This illustrates a fundamental problem, especially encountered in the processing and fabrication of ceramic materials in reproducing the same material from batch to batch.

At 1000°C, the material showed a distinctly different behaviour to that seen at 800 and 900°C. A total of eight specimens were tested and the majority failed in short duration. At 413 MPa, two specimens failed in 0.017 h (1 min) and 0.034 h (2 min), and the fracture surfaces showed [11] that the fast fracture was promoted by surface-associated oxidation, the presence of metallic inclusions (iron) and fine porosity in the material. As the stress was decreased to 344 MPa, the time-to-failure increased and varied from 1 to 3 h. Both specimens showed signs of early oxidation and

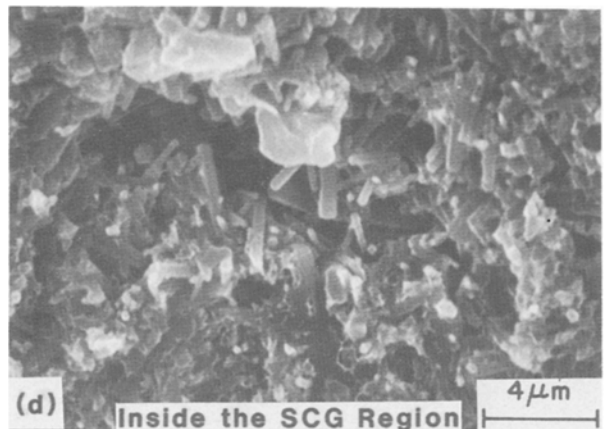
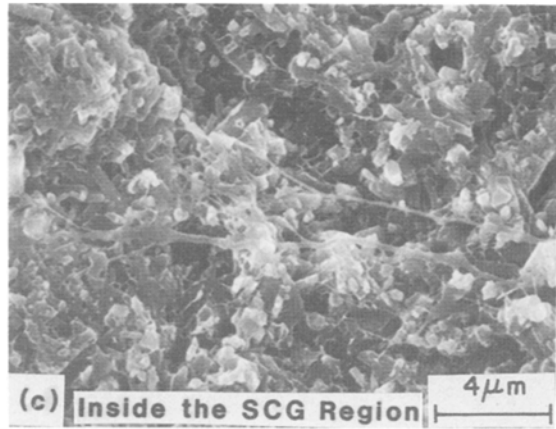
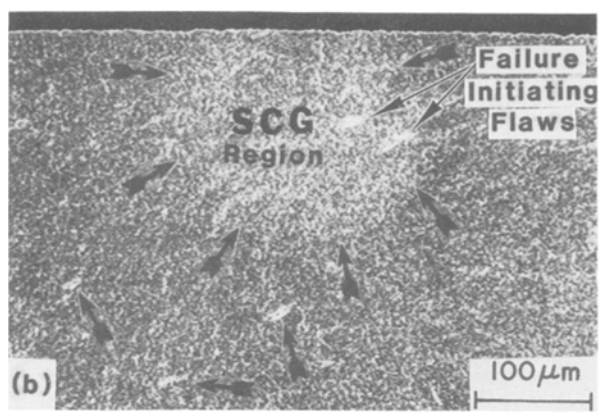
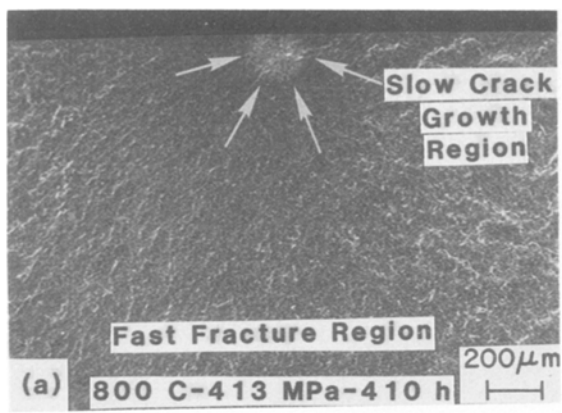


Figure 8 (a–d) SEM fractographs showing failure initiation and subsequent development of an SCG region in a specimen tested in stress rupture mode at 800°C.

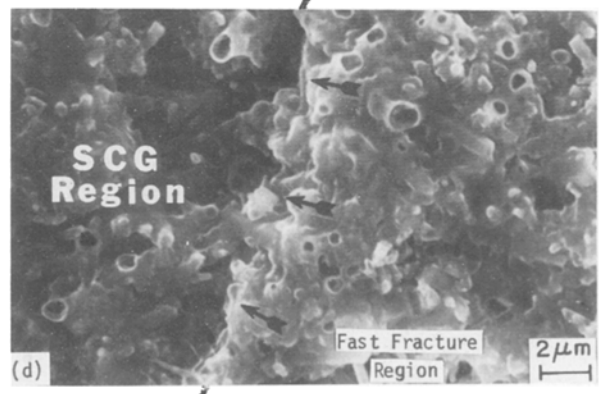
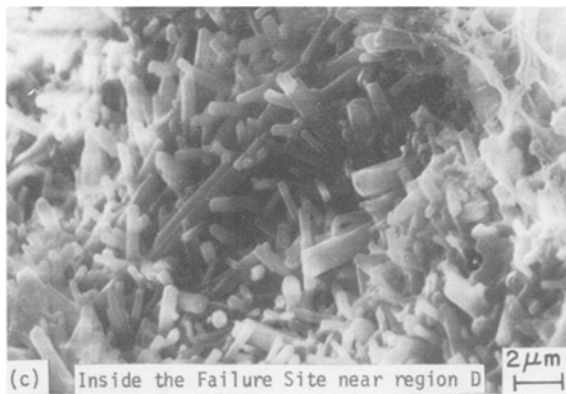
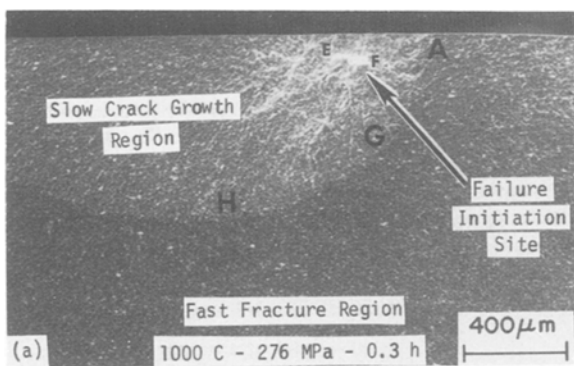


Figure 9 (a–d) SEM fractographs showing failure initiation and subsequent formation of a large SCG region in a specimen tested in stress rupture mode at 1000°C. AGH identifies the boundary of the SCG region and transition to fast fracture.

large regions of SCG [11]. Decreasing the applied stress further to 276 MPa did not seem to alter the creep deformation behaviour of the material. Of the three specimens tested, two failed in 0.1 and 0.3 h and one sustained the stress for 425 h without failure but displayed fine bending [11]. It should be pointed out that in spite of the fact that the applied stress of 276 MPa was significantly low compared to the average fast fracture strength ( $\sigma_f = 438$  MPa at 1000°C) (Fig. 4), yet the test specimen which failed in 0.3 h clearly displayed a large region of SCG (Fig. 9). The failure initiation site (Fig. 9a) appeared to be a processing defect (Figs 9b and c), similar to that seen in the fast fracture mode (Fig. 6). The mode of fracture during SCG was primarily intergranular (Fig. 9d), and outside the SCG region it was primarily transgranular (Fig. 9d) or a mixture of transgranular and intergranular crack propagation depending on the test temperature (Fig. 7). The transition from an intergranular mode of SCG to a transgranular cleavage mode accompanying high-speed fracture indicates that a fine balance exists between the alternate crack paths. In high-speed fracture, plastic deformation integral to crack growth is minimized due to the very high strain rate in the vicinity of the crack tip, and the crack finds a transgranular path easier than a more deformation-accommodating grain-boundary region. During SCG, the crack extends by plastic separation of what appears to behave as a ductile, low-viscosity grain-boundary glass phase, at stress levels considerably less than that necessary to promote transgranular fast fracture. When the stress intensity at the tip of the crack has increased sufficiently due to crack lengthening by SCG, a point is reached beyond which fast, transgranular fracture is more favourable (the Griffith condition is satisfied) and a transition to high-speed catastrophic fracture occurs as seen in Figs 7 to 9. At 1000°C, test specimens showed a distinct colour change (medium grey to white) and examination of the fracture surfaces showed the onset of oxidation.

#### 4. Summary

At room temperature, the fracture strength was dependent on crack length according to the Griffith criterion. Extrapolation of the data indicated that processing flaws (porosity, glassy particles and metallic (iron) contaminants) of 20 to 35  $\mu\text{m}$  were responsible for the brittle fracture of sintered silicon nitride containing various oxide additives (NGK-SN73). The fracture surface energy,  $\gamma$ , calculated at 20°C for fast fracture was about 73 J m<sup>-2</sup>.

The flexural strength was found to be independent of temperature from 20 to 800°C. Failure occurred in a brittle manner and the mode of crack propagation during fast fracture was primarily transgranular. The sudden decrease in strength at temperatures above 800°C was due to softening of the residual glass phase present in the material and led to the presence of SCG. The extent of SCG increased with increasing temperature. The mode of crack propagation during SCG was exclusively intergranular.

The use of precracked specimens containing cracks ranging in size from 50 to 100  $\mu\text{m}$  clearly showed the

importance of the temperature (1200°C) at which failure was governed by the extent of viscous flow of the glassy phase present in the material and not by the inherent flaw size.

Extensive flexural stress rupture evaluation in the temperature range 800 to 1000°C has identified the stress levels for time-dependent and time-independent failures. In addition, stress rupture testing at 800°C clearly revealed the early signs of viscous flow of the glassy phase and consequent degradation of the material strength.

#### Acknowledgements

It is a pleasure to thank K. Matsuhiro of NGK Laboratories for supplying some unpublished data on this material. Thanks are due to Dr Peter Beardmore for reviewing the paper and R. Goss for SEM work.

#### References

1. K. MATSUHITO and M. MATSUI, US Patent 4535063 (1985).
2. R. K. GOVILA, *J. Mater. Sci.* **20** (1985) 4345.
3. *Idem*, Technical Report TR 80-18 (Army Materials and Mechanics Research Center, Watertown, Massachusetts, 1980).
4. *Idem*, *J. Amer. Ceram. Soc.* **63** (1980) 319.
5. B. R. LAWN, A. G. EVANS and D. B. MARSHALL, *ibid.* **63** (1980) 574.
6. G. R. ANSTIS, P. CHANTIKUL, B. R. LAWN and D. B. MARSHALL, *ibid.* **64** (1981) 533.
7. P. CHANTIKUL, G. R. ANSTIS, B. R. LAWN and D. B. MARSHALL, *ibid.* **64** (1981) 539.
8. A. A. GRIFFITH, *Phil. Trans. R. Soc.* **A221** (1920) 163.
9. K. MATSUHITO, private communication (1983).
10. T. SOMA, M. MATSUI and I. ODA, paper presented at International Conference on Non-Oxide Technical and Engineering Ceramics, Limerick, Ireland, July 1985.
11. R. K. GOVILA, ASME Paper No. 87-GT-80. Gas Turbine Conference, Anaheim, California, June 1987.
12. R. R. WILLS, S. HOLMQUIST, J. M. WIMMER and J. A. CUNNINGHAM, *J. Mater. Sci.* **11** (1976) 1305.
13. F. F. LANGE, S. C. SINGHAL and R. C. KUZNICKI, *J. Amer. Ceram. Soc.* **60** (1977) 249.
14. K. W. BENN and W. D. CARRUTHERS, Third Quarterly Program Report, NASA Contract DEN 3-27 (AiResearch Mfg Co. of Arizona, 1978) p. 15.
15. N. J. TIGHE, K. KURODA, T. E. MITCHELL and A. H. HEUER, in "Electron Microscopy 1980", Vol. 4, edited by P. Brederoo and J. Van Landuyt (North-Holland, New York, 1980) pp. 310-313.
16. J. T. SMITH and C. L. QUACKENBUSH, *Amer. Ceram. Soc. Bull.* **59** (1980) 529.
17. *Idem*, *ibid.* **59** (1980) 533.
18. F. F. LANGE, *ibid.* **62** (1983) 1369.
19. R. K. GOVILA, J. A. MANGELS and J. R. BAER, *J. Amer. Ceram. Soc.* **68** (1985) 413.
20. R. K. GOVILA, *Amer. Ceram. Soc. Bull.* **65** (1986) 1287.
21. F. F. LANGE, *ibid.* **59** (1980) 239.
22. G. N. BABINI, A. BELLOSI and P. VINCENZINI, *J. Amer. Ceram. Soc.* **64** (1981) 578.
23. D. M. MIESKOWSKI and W. A. SANDERS, *ibid.* **68** (1985) C-160.
24. K. MATSUHITO, private communication (1986).

Received 1 April  
and accepted 16 June 1987